JM RAPIDS

Universality of dynamic flow structures in active viscoelastic liquids

Zhe Feng[1,2] [iD] **, Tiezheng Qian**[3] **and Rui Zhang**[1] [iD]

[1]Department of Physics, The Hong Kong University of Science and Technology, Clear Water Bay, Kowloon, Hong Kong

[2]Institute of High Performance Computing (IHPC), Agency for Science, Technology and Research (A∗STAR), 1 Fusionopolis Way, # 16–16 Connexis, Singapore 138632, Republic of Singapore

[3]Department of Mathematics, The Hong Kong University of Science and Technology, Clear Water Bay, Kowloon, Hong Kong

Corresponding author: Rui Zhang, ruizhang@ust.hk

Active fluids encompass a wide range of non-equilibrium fluids, in which the self-propulsion or rotation of their units can give rise to large-scale spontaneous flows. Despite the diversity of active fluids, they are commonly viscoelastic. Therefore, we develop a hydrodynamic model of isotropic active liquids by accounting for their viscoelasticity. Specifically, we incorporate an active stress term into a general viscoelastic liquid model to study the spontaneous flow states and their transitions in two-dimensional channel, annulus and disk geometries. We have discovered rich spontaneous flow states in a channel as a function of activity and Weissenberg number, including unidirectional flow, travelling-wave and vortex-roll states. The Weissenberg number acts against activity by suppressing the spontaneous flow. In an annulus confinement, we find that a net flow can be generated only if the aspect ratio of the annulus is not too large nor too small, akin to some three-dimensional active-flow phenomena. In a disk geometry, we observe a periodic chirality switching of a single vortex flow, resembling the bacteria-based active fluid experiments. The two phenomena reproduced in our model differ in Weissenberg number and frictional coefficient. As such, our active viscoelastic model offers a unified framework to elucidate diverse active liquids, uncover their connections and highlight the universality of dynamic active-flow patterns.

Key words: active matter

1. Introduction

Active matter represents a range of non-equilibrium systems comprising self-propelled units such as active particles (Datt & Elfring 2019; Maity & Burada 2022), bacteria, cells (Dombrowski *et al.* 2004; Sokolov *et al.* 2007; Dunkel *et al.* 2013) or biopolymers (Fürthauer *et al.* 2019; Lemma *et al.* 2021; Chandrakar *et al.* 2022; Zarei *et al.* 2023). Active fluids are a typical class of active matter which can form a gas or liquid phase or be suspended in another liquid. The constituents in an active fluid can convert other forms of energy into mechanical work by inducing stresses and interacting with the environment, such as driving flows in the background fluid, moving against neighbour units and undergoing phase separation. Active fluids are promising for emergent applications in biomedicine (Ghosh *et al.* 2020), robotics (Ceron *et al.* 2021) and materials science (Needleman & Dogic 2017), and have the potential to revolutionise our understanding of how living systems operate and to provide new design principles for biomimetic, functional and autonomous materials (Zhang *et al.* 2021). However, our current understanding of their dynamic behaviours is still overwhelmed by the microscopic details of the specific system.

A paradigmatic class of active fluids is active liquid crystals (LCs) (Zhang *et al.* 2021), which comprise locally aligned dense units with anisotropic shapes, forming different LC phases in non-equilibrium conditions. One of such active LC phases is namely active nematic (Doostmohammadi *et al.* 2018), which widely exists in many biological and synthetic systems (Narayan, Ramaswamy & Menon 2007; Sanchez *et al.* 2012; Zhou *et al.* 2014; Kawaguchi, Kageyama & Sano 2017; Saw *et al.* 2017; Kumar *et al.* 2018; Li *et al.* 2019). Though active LC systems are diverse, their spontaneous flows can be well understood by a hydrodynamic model (Denniston, Orlandini & Yeomans 2001; Marenduzzo *et al.* 2007*a*), in which active stresses drive positive topological defects into self-propulsion (Aditi Simha & Ramaswamy 2002; Shankar *et al.* 2018). Nevertheless, the success of the hydrodynamic model of active LCs cannot be extended directly to active fluids without LC order (Marchetti *et al.* 2013), in which a nematic director field does not exist.

In the present work, we propose an active viscoelastic model in an attempt to provide a unified framework to describe distinct isotropic active fluids. Here we focus on two experimental systems. One is microtubule-based active fluids, in which the active motion of the kinesin motor clusters can lead to the relative slidings of microtubule bundles, driving different spontaneous flow patterns tuneable by confinement geometry (Wu *et al.* 2017). The other active fluid is bacterial suspensions (Liu *et al.* 2021; Nishiguchi *et al.* 2024). In addition to geometric confinements (Wioland, Lushi & Goldstein 2016; Bhattacharjee & Datta 2019), the inclusion of different amounts of DNA molecules in the bacteria-based active fluid can also be used to control its flow state via tuning its viscoelasticity (Liu *et al.* 2021). As DNA concentration increases, the spontaneous flow in a disk can transition from a turbulent-like state to a unidirectional giant vortex, and to an oscillatory mode in which a single vortex flow can periodically switch between clockwise (CW) and counter-clockwise (CCW) directions (Liu *et al.* 2021). Despite the richness of the flow patterns observed in these different isotropic active fluidic systems, little is known about the universality of these flow patterns and how they depend on the system specifics.

The hydrodynamic model of active LCs has been used to understand isotropic active fluids in both two-dimensional (2-D) (Fielding, Marenduzzo & Cates 2011; Caballero, You & Marchetti 2023) and three-dimensional (3-D) geometries (Chandragiri *et al.* 2020;
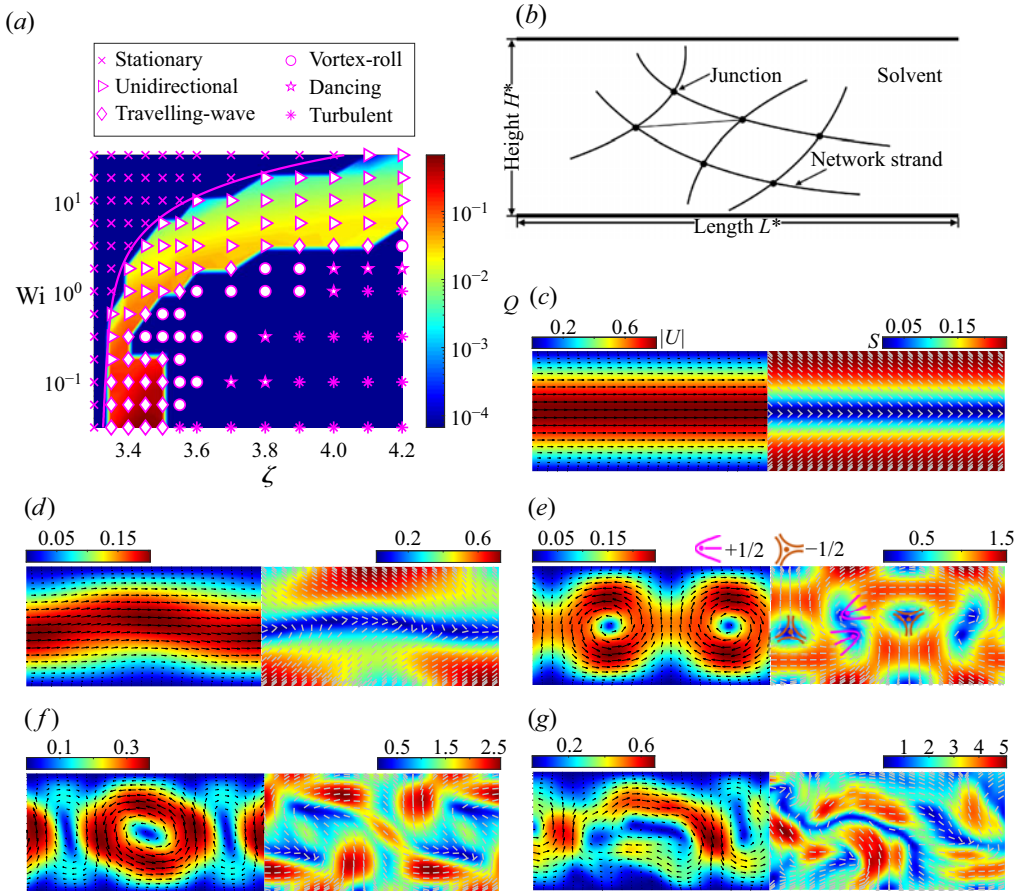
Figure 1. Flow state transitions of an active viscoelastic fluid in a 2-D channel. (*a*) Flow state diagram in terms of the activity ζ and Weissenberg number Wi. The background colour represents the magnitude of the time-averaged flow rate Q. The solid magenta line marks ζ_c obtained by linear stability analysis. (*b*) Schematic of the network structure for the PTT model. (*c*) Unidirectional flow state (Wi $= 10^{-0.5}$, $\zeta = 3.35$). The left half-part of the channel shows the velocity field **U** with background colour indicating the magnitude |**U**|. The other half-part shows the orientation **r** of the polymer molecules and their order magnitude S. (*d*) Travelling-wave state (Wi $= 10^{-0.5}$, $\zeta = 3.4$). (*e*) Vortex-roll state (Wi $= 10^{-0.5}$, $\zeta = 3.5$). $\pm 1/2$ defects are present. (*f*) Dancing state (Wi $= 10^{-0.5}$, $\zeta = 3.8$). (*g*) Turbulent-like state (Wi $= 10^{-0.5}$, $\zeta = 4.2$).

Varghese *et al.* 2020). In these models, a nematic order parameter is required. For many polymer-based viscoelastic liquids, however, there is no LC ordering but instead require a stress tensor.

In this study, we try to ask whether a hydrodynamic model of active fluids without LC order can be used to describe various isotropic active fluidic phenomena. To this end, we modify a viscoelastic liquid model by including an active stress term (Aditi Simha & Ramaswamy 2002). We then use the model to study different 2-D confinement geometries. Our model produces rich spontaneous flow states (see figure 1*a*) and can reproduce distinct dynamical flow patterns observed in the various experiments, which we elaborate in the following.

2. Problem formulation

2.1. *Governing equations*

We simulate a 2-D active viscoelastic fluid using the Phan-Thien–Tanner (PTT) model (Thien & Tanner 1977; Phan-Thien 1978) in which the constitutive equation is derived from a network theory for polymeric liquids (see figure 1*b*). The network junctions in this model are allowed to exhibit a certain degree of effective slip relative to the background continuum, and the relaxation time is assumed to be dependent on the local stress. The dimensionless governing equations of the active viscoelastic system (derivation presented in the supplementary material available at https://doi.org/10.1017/jfm.2025.177) consist of the incompressible Navier–Stokes equation and the constitutive equation:

$$\nabla \cdot \mathbf{U} = 0, \tag{2.1a}$$

$$\frac{\partial \mathbf{U}}{\partial t} = -\nabla P + \nabla^2 \mathbf{U} + \frac{1-\beta}{\beta}(1-\zeta)\nabla \cdot \boldsymbol{\tau} - \nu \mathbf{U}, \tag{2.1b}$$

$$\frac{\partial \boldsymbol{\tau}}{\partial t} + \mathbf{U} \cdot \nabla \boldsymbol{\tau} + \xi\left(\boldsymbol{\tau} \cdot \mathbf{D} + \mathbf{D} \cdot \boldsymbol{\tau}\right) - \boldsymbol{\tau} \cdot \nabla \mathbf{U} - [\boldsymbol{\tau} \cdot (\nabla \mathbf{U})]^T = \frac{2}{\mathrm{Wi}}\mathbf{D} - \frac{f(\tau_{kk})}{\mathrm{Wi}}\boldsymbol{\tau} + \kappa \nabla^2 \boldsymbol{\tau}, \tag{2.1c}$$

where P denotes pressure, and $\mathbf{U}$ and $\boldsymbol{\tau}$ are the velocity vector and polymer-induced symmetric stress tensor, respectively. Here $\mathbf{D} = [\nabla \mathbf{U} + (\nabla \mathbf{U})^T]/2$ is the rate-of-strain tensor. The two dimensionless control parameters are the Weissenberg number $\mathrm{Wi} = U_c \lambda / L_c$ with $U_c = \eta_s/(\rho_0 L_c)$, where ν is the friction coefficient and ρ_0 denotes the liquid density, and the viscosity ratio $\beta = \eta_s/(\eta_s + \eta_p)$, where λ is the polymer relaxation time for $\tau_{kk} \to 0$, L_c represents a characteristic length of the system, τ_{kk} refers to the trace of the stress tensor, and η_s and η_p are the contributions to viscosity from the solvent and the polymer, respectively. To account for activity of the self-propelled units, we adopt an active stress term $-\zeta \boldsymbol{\tau}$ that is linear with respect to the stress tensor, which implies that any anisotropy in the conformation of the polymer can induce an anisotropic stress that enhances such anisotropy; this term is similar to the swim pressure proposed by Omar, Wang & Brady (2020) and the active stress term in the active LC theory (Marenduzzo *et al.* 2007*b*). The effect of substrate friction from the third dimension is described by $-\nu \mathbf{U}$ in equation (2.1*b*). We consider Stokes limit by dropping the non-linear inertial term in equation (2.1*b*). An artificial diffusion term $\kappa \nabla^2 \boldsymbol{\tau}$ is introduced in equation (2.1*c*) to enhance numerical stability (here $\kappa = 10^{-3}$). In the PTT model, the dimensionless parameter ξ ($0 < \xi < 1$) accounts for the slip between the network and the background continuous medium. Additionally, the linear relaxation function $f(\tau_{kk}) = 1 + \epsilon \mathrm{Wi}\tau_{kk}$ (Thien & Tanner 1977) is used, where the dimensionless parameter ϵ controls the extensibility of the polymer (Thien & Tanner 1977) which is different from the constant molecular length in the active LC model. In addition, compared with the pure active LC model (Marenduzzo *et al.* 2007*b*) and the combined model for active LCs and viscoelastic polymers (Hemingway *et al.* 2015), the governing equations (2.1) have different forms, particularly in the momentum equation.

2.2. *Simulation details*

The governing equations (2.1) are numerically solved using the open-source pseudo-spectral package Dedalus (Burns *et al.* 2020). The Fourier basis is applied for the periodic directions and the Chebyshev polynomials for the wall-normal direction. The time integration is performed using the RK222 scheme which is a second-order, two-step,

implicit/explicit Runge–Kutta method. On the wall, a no-slip boundary condition is used for the velocity field, and a Neumann condition $\partial \boldsymbol{\tau}/\partial w_\perp = 0$ is used for the polymer stress, with $w_\perp$ denoting the wall-normal direction. In contrast to LC models, here no preferred molecular alignment direction is imposed on the boundary. All the simulations reported here are started with zero velocity and a randomised polymer stress of small magnitude. The flow rate Q is defined by $Q = \iint U_\| d\mathbf{x}/\mathfrak{V}$, where $U_\|$ denotes the velocity component parallel to the wall, and $\mathfrak{V}$ denotes the volume of the system. Here Q is used as an order parameter to distinguish the coherent and turbulent flow states. When $Q \neq 0$, a coherent flow emerges. In the following, the viscosity ratio is set to $\beta = 0.7$ which is close to the experimental observations (Wu *et al.* 2017; Gagnon *et al.* 2020). The active viscoelastic fluid is assumed to exhibit a strong slip effect and weak extensibility, with parameters $\xi = 0.7$ and $\epsilon = 10^{-2}$. The friction force is not considered (i.e. $\nu = 0$) unless specified otherwise.

3. Results

3.1. *Channel geometry*

We start with a flat channel with lateral length $L = 4$ and grid resolution $N_x \times N_y = 144 \times 36$. Above a critical activity ζ_c, there is an onset of a spontaneous flow (i.e. unidirectional flow) as shown in figure 1(*a*). Weissenberg number is defined as $\text{Wi} = \eta_s \lambda/\{\rho_0 L_c^2\}$ (with $L_c = H^*$ in figure 1(*b*), the dimensionless channel height would be 1). As Wi increases, ζ_c becomes higher, which is consistent with our linear stability analysis (the solid magenta line in figure 1*a*) as well as the mixed model of LC and viscoelastic liquids (Hemingway *et al.* 2015). Note that ζ_c approaches a constant value at a vanishing Wi. This limit can be understood by considering an unconfined 2-D domain. Indeed, our stability analysis of an infinite 2-D domain shows that ζ_c is only determined by the viscosity ratio, namely $\zeta_c = 1/(1 - \beta)$ (see supplementary material). For $\beta = 0.7$ used in the simulation, the critical activity $\zeta_c = 1/(1 - \beta) \approx 3.3$ agrees quantitatively well with the vanishing Wi result in figure 1(*a*).

As activity further increases, the steady unidirectional flow sequentially transitions into travelling-wave, vortex-roll, dancing and finally turbulent state at the highest ζ as shown in figure 1(*c–g*) (see supplementary movie 1). Many of these 2-D channel flow states except the vortex-roll state are also found in active nematic models (Shendruk *et al.* 2017; Chandragiri *et al.* 2019). In the unidirectional flow state, the flow rate Q increases as activity ζ increases. Upon further increase of ζ, Q drops abruptly as the system transitions into the travelling-wave state, in which the spontaneous flow starts to develop in the vertical direction. Owing to the random initial conditions of the stress tensor field, rightward and leftward flows in the unidirectional and travelling-wave states can be observed in our simulation with equal probability (see supplementary material). Based on the linear stability analysis (see supplementary material), the wavelength l_{tw} of the travelling-wave state increases with Wi and decreases with ζ as shown in figures 2(*a*) and 2(*b*). In the vortex-roll state, the stretching of the polymers gives rise to a birefringent field, in which $\pm 1/2$ defects can be identified (see figure 1*e*), and this resembles active nematic systems (Zhang *et al.* 2021). The $\pm 1/2$ topological defects refer to regions where the principal axis corresponding to the largest eigenvalue of the local stress tensor changes abruptly, which is similar to that seen in nematic LCs. The development of the local nematic order has also been observed in 3-D microtubule suspensions (Wu *et al.* 2017).
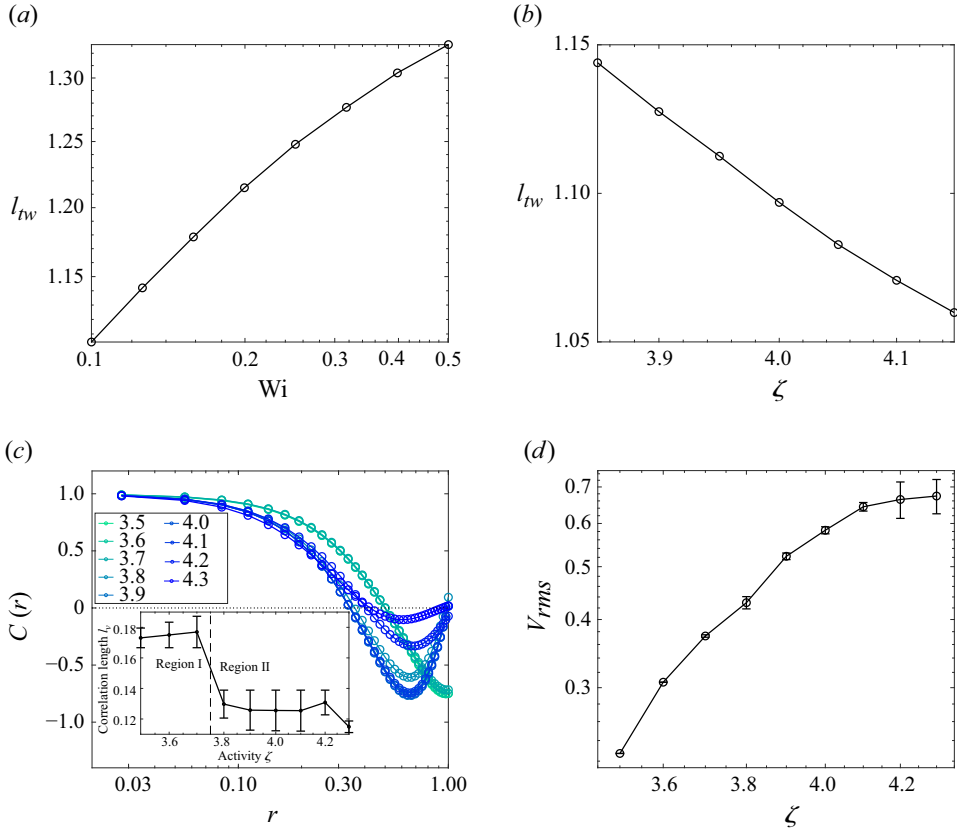
Figure 2. Effect of (*a*) Weissenberg number Wi and (*b*) activity ζ on the wavelength l_{tw} in the travelling-wave state in the 2-D channel by linear stability analysis (see supplementary material). Here $\zeta = 3.4$ in (*a*) and Wi $= 10^{0.5}$ in (*b*). (*c*) Normalised velocity-velocity correlation function $C(r)$ at different activity ζ. The inset shows the velocity correlation length l_v determined by $C = 0.8$. Region I denotes the vortex-roll state, and region II represents the dancing and turbulent states. (*d*) Effect of ζ on the r.m.s. velocity, V_{rms}. The error bars denote the standard deviation for time series of r.m.s. velocity. In (*c,d*), the Weissenberg number is Wi $= 10^{-0.5}$.

Figure 2(*c*) shows the effect of activity ζ on the normalised velocity-velocity correlation function $C(r) = \langle \mathbf{U}(r) \cdot \mathbf{U}(0) \rangle / \langle \mathbf{U}(0)^2 \rangle$, where r denotes the dimensionless horizontal distance and $\langle \cdot \rangle$ denotes the ensemble (spatio–temporal) average. The velocity correlation length l_v is found to be independent of ζ except at the transition from the vortex-roll into the turbulent state, at which l_v undergoes an abrupt decrease. Such a feature is also observed in the active microtubule experiment (Sanchez *et al.* 2012) and in nematic LC models (Thampi, Golestanian & Yeomans 2013). Additionally, the measured root-mean-square (r.m.s.) velocity V_{rms} saturates at high ζ as presented in figure 2(*d*) which is consistent with the experiments (Sanchez *et al.* 2012; Henkin *et al.* 2014; Tan *et al.* 2019), while the nematic LC model did not exhibit such saturation trend (Thampi *et al.* 2013).

3.2. *Annulus geometry*

In the annulus geometry, the aspect ratio is defined by $\Gamma = R_i/R_o$, where R_i and R_o denote the inner and outer radii, respectively. The grid resolution is set to
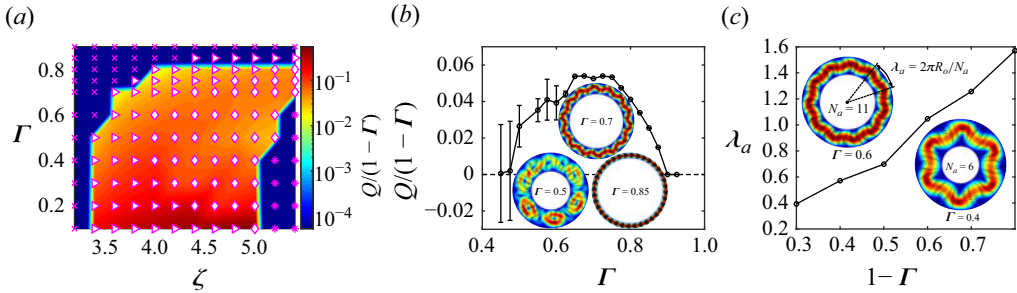
Figure 3. Flow state transitions of an active viscoelastic fluid in a 2-D annulus. (*a*) Flow state diagram in terms of ζ and aspect ratio Γ at Wi = 1. (*b*) Effect of aspect ratio Γ on the average flow rate at $\zeta = 5.2$. The error bars denote the standard deviation of time series for flow rate. (*c*) Variation of the arc wavelength λ_a with the thickness $(1 - \Gamma)$ of the annulus at $\zeta = 4.4$. The inset contour denotes the velocity magnitude under different aspect ratio Γ, which helps to identify the number of repeated arc segments, N_a.

$N_\theta \times N_r = 216 \times 36$. Here the outer radius is chosen as the characteristic length, namely $L_c = R_o$. This geometry parameter $\Gamma \in (0, 1)$ can be used to investigate the effect of geometric confinement on the flow states. Different from the channel geometry, the annulus geometry exhibits stationary, unidirectional, travelling-wave and turbulent states only as shown in figure 3(*a*), consistent with the previous numerical results which were obtained for 2-D apolar active suspension confined in an annulus by using a coarse-grained LC model (Chen, Gao & Gao 2018). As Γ increases, the confinement becomes stronger, and the system undergoes transitions from the turbulent flow into the travelling-wave state and into the unidirectional flow state (see figure 3*a,b*). Figure 3(*b*) shows that for $\Gamma \to 1$ (thin annulus) or $\Gamma \to 0$ (wide annulus), the system is in the stationary or the turbulent state, in which a net flow vanishes. Note that in a 3-D experiment of a microtubule-based active fluid, the flow rate also shows a non-monotonic dependence on the aspect ratio of the confinement (Wu *et al.* 2017). Because the azimuthal direction of the annulus requires periodicity, the wavelength of the travelling-wave state should be a fraction of the lateral length. As shown in figure 3(*c*), it is observed that such wavelength λ_a increases with the increasing width $1 - \Gamma$, consistent with experimental results (Chandrakar *et al.* 2020).

3.3. *Disk geometry*

Next we study disk confinement where its radius is taken as the characteristic length L_c, and the grid resolution is $N_\theta \times N_r = 216 \times 36$. Different from the previous two geometries, a disk only has one single wall which may induce more interesting flow phenomena. Similar to that in a channel, the active flow in a disk also tends to be turbulent at high ζ and small Wi (see supplementary material for the flow state diagram of the disk geometry). This effect of Wi agrees well with the experimental result for low DNA concentration (and hence small Wi) reported in Liu *et al.* (2021). The effective friction due to the confining substrates can tune the flow structure in active fluids (Liu *et al.* 2021; Caballero *et al.* 2023). Here we incorporate it into our model by setting $\nu = 1.1$. We observe the flow which shows periodic chirality switching, with one full-scale vortex followed by the next one with opposite chirality (see figure 4(*c*) and supplementary movie 2). Moreover, the chirality switching shows a frequency that decreases as Wi increases, which is proportional to the polymer relaxation time as shown in figure 4(*a*). The detailed process of switching from CW to CCW vortex is presented in figure 4(*c*).
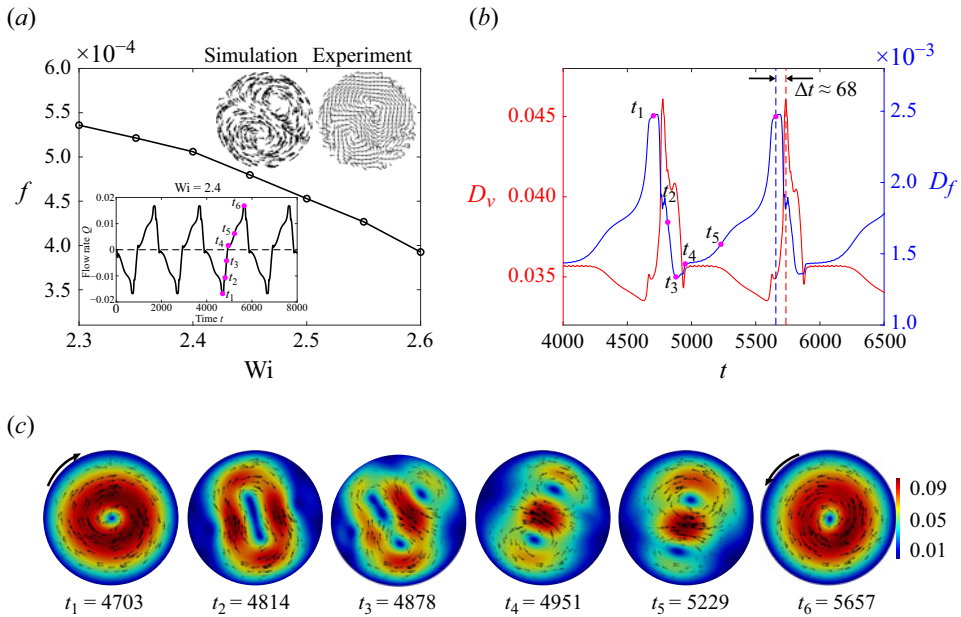
(a) (b)

(c)

Figure 4. Chirality-switching vortex flows of the active viscoelastic fluid in a 2-D disk. (*a*) Chirality-switching frequency f as a function of Wi at $\zeta = 4.5$. The friction coefficient is set to $\nu = 1.1$. The bottom-left inset shows the time series of Q at Wi $= 2.4$, and the top-right inset shows the transient two-vortex structure in our model and in former experiment (Liu *et al.* 2021). (*b*) Temporal evolution of viscous dissipation rate and frictional dissipation rate. (*c*) Sequential snapshots show the chirality switching from CW to CCW. The colour indicates velocity magnitude.

The system is started with a full-scale CW vortex at t_1, which gradually decays (at t_2), while a secondary CCW vortex is formed close to the wall (at t_3). The decay of the CW vortex progresses. Concomitantly, the CCW vortex continues to grow (at t_4 and t_5). Finally, the CCW vortex reaches its full scale (at t_6). It is interesting to note that the centres of the vortices also rotate, first in the CW sense (before t_4) and then in the CCW sense (after t_4). This chirality switching repeats periodically. These numerical observations agree well with the experiment of bacterial active fluids, where the switching can be made slower by adding more DNAs into the fluid (Liu *et al.* 2021). A similar chirality-reversal vortex flow was observed in a microtubule-based active nematic confined to a disk region; however, the reversal does not appear to persist periodically (Opathalage *et al.* 2019). Figure 4(*b*) shows the frictional dissipation rate $D_f = \nu \int |\mathbf{U}|^2 \mathrm{d}\mathbf{x}$ and the viscous dissipation rate $D_v = \frac{1}{2} \int [\nabla \mathbf{U} + (\nabla \mathbf{U})^T] : [\nabla \mathbf{U} + (\nabla \mathbf{U})^T] \mathrm{d}\mathbf{x}$, and their time variations are consistent with a fast decrease of the absolute flow rate $|Q|$ from a peak (from t_1 to t_3) followed by a relatively slow increase of $|Q|$ toward the next peak (from t_4 to t_6). A proper orthogonal decomposition (POD) analysis (Berkooz, Holmes & Lumley 1993) of the vorticity field reveals that the dominant modes are 1-, 2- and 4-vortex flows as shown in figure 5 which is consistent with a recent bacterial active fluid experiment (Nishiguchi *et al.* 2024). Using different ζ and Wi, our system can generate chirality-switching flows with more vortices (see supplementary material). As Wi decreases, a transition from 2-vortex to 4-vortex state can take place, again in good agreement with the bacteria experiment (Nishiguchi *et al.* 2024). A similar periodic flow reversal phenomenon was
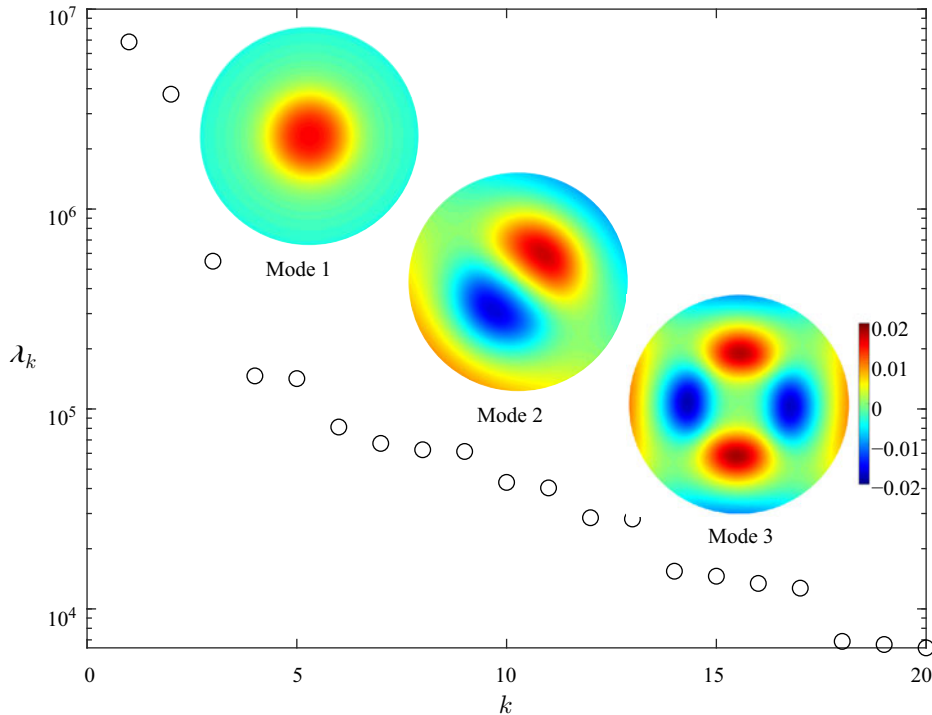
Figure 5. Energy of different modes for chirality-switching vortex flows of the active viscoelastic fluid in a 2-D disk with $\nu = 1.1$, $\zeta = 4.5$ and Wi $= 2.4$. Inset shows the first three modes obtained by the POD analysis.

predicted in a channel of an active nematic sandwiched between two viscoelastic layers (Mori *et al.* 2023).

4. Conclusion

We have developed an active viscoelastic liquid model to describe active liquids without LC order. We studied its spontaneous flow patterns in 2-D channel, annulus and disk geometries. In addition to the geometric confinement (i.e. aspect ratio of annulus here), the current model is also capable of controlling the flow state by Weissenberg number which is one macroscopic parameter measuring the viscoelasticity of the liquid. Our model features a different mathematical form compared with existing models, and it can reproduce active-flow patterns and characteristics typical of distinct experimental systems within a single framework. Therefore, we argue that flow patterns observed in bacteria-based systems, e.g. periodic chirality-switching flow, should also occur in microtubule-based systems, and *vice versa*: the non-monotonic dependence of channel flow on aspect ratio found in microtubule-based systems should also be found in bacteria-based systems (Wioland *et al.* 2016). Note that for gel-like active LCs exhibiting a nematic or polar order (Hemingway *et al.* 2015, 2016), the well-developed active LC model will be needed. In addition, the present 2-D simulations are unable to explicitly capture the inherently 3-D phenomena observed in isotropic active fluids except for quasi-2-D phenomena which can be reproduced through the addition of a frictional term to account for the viscous damping by the confining walls in the third direction. In future work, we plan to extend

our research to 3-D systems, leveraging the inherently 3-D nature of the PTT model used in current work. Furthermore, exploring the influence of pre-defined polymer orientations at the boundaries also offers a compelling direction for further investigation.

Declaration of interests. The authors report no conflict of interest.

REFERENCES

ADITI SIMHA, R. & RAMASWAMY, S. 2002 Hydrodynamic fluctuations and instabilities in ordered suspensions of self-propelled particles. *Phys. Rev. Lett.* **89** (5), 058101.

BERKOOZ, G., HOLMES, P. & LUMLEY, J. 1993 The proper orthogonal decomposition in the analysis of turbulent flows. *Annu. Rev. Fluid Mech.* **25** (1), 539–575.

BHATTACHARJEE, T. & DATTA, S. 2019 Confinement and activity regulate bacterial motion in porous media. *Soft Matter* **15** (48), 9920–9930.

BURNS, K.J., VASIL, G.M., OISHI, J.S., LECOANET, D. & BROWN, B.P. 2020 Dedalus: a flexible framework for numerical simulations with spectral methods. *Phys. Rev. Res.* **2** (2), 023068.

CABALLERO, F., YOU, Z. & MARCHETTI, M. 2023 Vorticity phase separation and defect lattices in the isotropic phase of active liquid crystals. *Soft Matter* **19** (40), 7828–7835.

CERON, S., KIMMEL, M.A., NILLES, A. & PETERSEN, K. 2021 Soft robotic oscillators with strain-based coordination. *IEEE Robot. Autom. Lett.* **6** (4), 7557–7563.

CHANDRAGIRI, S., DOOSTMOHAMMADI, A., YEOMANS, J.M. & THAMPI, S.P. 2019 Active transport in a channel: stabilisation by flow or thermodynamics. *Soft Matter* **15** (7), 1597–1604.

CHANDRAGIRI, S., DOOSTMOHAMMADI, A., YEOMANS, J.M. & THAMPI, S.P. 2020 Flow states and transitions of an active nematic in a three-dimensional channel. *Phys. Rev. Lett.* **125** (14), 148002.

CHANDRAKAR, P. *et al.* 2022 Engineering stability, longevity, and miscibility of microtubule-based active fluids. *Soft Matter* **18** (9), 1825–1835.

CHANDRAKAR, P., VARGHESE, M., AGHVAMI, S., BASKARAN, A., DOGIC, Z. & DUCLOS, G. 2020 Confinement controls the bend instability of three-dimensional active liquid crystals. *Phys. Rev. Lett.* **125** (25), 257801.

CHEN, S., GAO, P. & GAO, T. 2018 Dynamics and structure of an apolar active suspension in an annulus. *J. Fluid Mech.* **835**, 393–405.

DATT, C. & ELFRING, G.J. 2019 Active particles in viscosity gradients. *Phys. Rev. Lett.* **123** (15), 158006.

DENNISTON, C., ORLANDINI, E. & YEOMANS, J. 2001 Lattice Boltzmann simulations of liquid crystal hydrodynamics. *Phys. Rev. E* **63** (5), 056702.

DOMBROWSKI, C., CISNEROS, L., CHATKAEW, S., GOLDSTEIN, R.E. & KESSLER, J.O. 2004 Self-concentration and large-scale coherence in bacterial dynamics. *Phys. Rev. Lett.* **93** (9), 098103.

DOOSTMOHAMMADI, A., IGNÉS-MULLOL, J., YEOMANS, J.M. & SAGUÉS, F. 2018 Active nematics. *Nat. Commun.* **9** (1), 3246.

DUNKEL, J., HEIDENREICH, S., DRESCHER, K., WENSINK, H.H., BÄR, M. & GOLDSTEIN, R.E. 2013 Fluid dynamics of bacterial turbulence. *Phys. Rev. Lett.* **110** (22), 228102.

FIELDING, S.M., MARENDUZZO, D. & CATES, M.E. 2011 Nonlinear dynamics and rheology of active fluids: simulations in two dimensions. *Phys. Rev. E* **83** (4), 041910.

FÜRTHAUER, S., LEMMA, B., FOSTER, P J., EMS-MCCLUNG, S.C., YU, C.-H., WALCZAK, C.E., DOGIC, Z., NEEDLEMAN, D.J. & SHELLEY, M.J. 2019 Self-straining of actively crosslinked microtubule networks. *Nat. Phys.* **15** (12), 1295–1300.

GAGNON, D.A., DESSI, C., BEREZNEY, J.P., BOROS, R., CHEN, D. T.-N., DOGIC, Z. & BLAIR, D.L. 2020 Shear-induced gelation of self-yielding active networks. *Phys. Rev. Lett.* **125** (17), 178003.

GHOSH, A., XU, W., GUPTA, N. & GRACIAS, D.H. 2020 Active matter therapeutics. *Nano Today* **31**, 100836.

HEMINGWAY, E., MAITRA, A., BANERJEE, S., MARCHETTI, M., RAMASWAMY, S., FIELDING, S.M. & CATES, M.E. 2015 Active viscoelastic matter: from bacterial drag reduction to turbulent solids. *Phys. Rev. Lett.* **114** (9), 098302.

HEMINGWAY, E J., CATES, M. & FIELDING, S.M. 2016 Viscoelastic and elastomeric active matter: linear instability and nonlinear dynamics. *Phys. Rev. E* **93** (3), 032702.

HENKIN, G., DECAMP, S. J., CHEN, D. T., SANCHEZ, T. & DOGIC, Z. 2014 Tunable dynamics of microtubule-based active isotropic gels. *Phil. Trans. R. Soc. Lond. A* **372** (2029), 20140142.

KAWAGUCHI, K., KAGEYAMA, R. & SANO, M. 2017 Topological defects control collective dynamics in neural progenitor cell cultures. *Nature* **545** (7654), 327–331.

KUMAR, N., ZHANG, R., DE, P., JUAN, J. & GARDEL, M.L. 2018 Tunable structure and dynamics of active liquid crystals. *Sci. Adv.* **4** (10), eaat7779.

LEMMA, L.M., NORTON, M.M., TAYAR, A.M., DECAMP, S.J., AGHVAMI, S., FRADEN, S., HAGAN, M.F. & DOGIC, Z. 2021 Multiscale microtubule dynamics in active nematics. *Phys. Rev. Lett.* **127** (14), 148001.

LI, H., SHI, X.-Q., HUANG, M., CHEN, X., XIAO, M., LIU, C., CHATÉ, H. & ZHANG, H. 2019 Data-driven quantitative modeling of bacterial active nematics. *Proc. Natl. Acad. Sci. USA* **116** (3), 777–785.

LIU, S., SHANKAR, S., MARCHETTI, M. & WU, Y. 2021 Viscoelastic control of spatiotemporal order in bacterial active matter. *Nature* **590** (7844), 80–84.

MAITY, R. & BURADA, P. 2022 Unsteady chiral swimmer and its response to a chemical gradient. *J. Fluid Mech.* **940**, A13.

MARCHETTI, M., JOANNY, J.-F., RAMASWAMY, S., LIVERPOOL, T.B., PROST, J., RAO, M. & SIMHA, R. 2013 Hydrodynamics of soft active matter. *Rev. Mod. Phys.* **85** (3), 1143–1189.

MARENDUZZO, D., ORLANDINI, E., CATES, M. & YEOMANS, J. 2007*a* Steady-state hydrodynamic instabilities of active liquid crystals: hybrid lattice Boltzmann simulations. *Phys. Rev. E* **76** (3), 031921.

MARENDUZZO, D., ORLANDINI, E. & YEOMANS, J. 2007*b* Hydrodynamics and rheology of active liquid crystals: a numerical investigation. *Phys. Rev. Lett.* **98** (11), 118102.

MORI, F., BHATTACHARYYA, S., YEOMANS, J.M. & THAMPI, S.P. 2023 Viscoelastic confinement induces periodic flow reversals in active nematics. *Phys. Rev. E* **108** (6), 064611.

NARAYAN, V., RAMASWAMY, S. & MENON, N. 2007 Long-lived giant number fluctuations in a swarming granular nematic. *Science* **317** (5834), 105–108.

NEEDLEMAN, D. & DOGIC, Z. 2017 Active matter at the interface between materials science and cell biology. *Nat. Rev. Mater.* **2** (9), 1–14.

NISHIGUCHI, D., SHIRATANI, S., TAKEUCHI, K. A. & ARANSON, I. S. 2024 Vortex reversal is a precursor of confined bacterial turbulence. arXiv preprint arXiv:2407.05269.

OMAR, A.K., WANG, Z.-G. & BRADY, J.F. 2020 Microscopic origins of the swim pressure and the anomalous surface tension of active matter. *Phys. Rev. E* **101** (1), 012604.

OPATHALAGE, A., NORTON, M.M., JUNIPER, M.P., LANGESLAY, B., AGHVAMI, S., FRADEN, S. & DOGIC, Z. 2019 Self-organized dynamics and the transition to turbulence of confined active nematics. *Proc. Natl. Acad. Sci. USA* **116** (11), 4788–4797.

PHAN-THIEN, N. 1978 A nonlinear network viscoelastic model. *J. Rheol.* **22** (3), 259–283.

SANCHEZ, T., CHEN, D.T.N., DECAMP, S.J., HEYMANN, M. & DOGIC, Z. 2012 Spontaneous motion in hierarchically assembled active matter. *Nature* **491** (7424), 431–434.

SAW, T.B., DOOSTMOHAMMADI, A., NIER, V., KOCGOZLU, L., THAMPI, S., TOYAMA, Y., MARCQ, P., LIM, C.T., YEOMANS, J.M. & LADOUX, B. 2017 Topological defects in epithelia govern cell death and extrusion. *Nature* **544** (7649), 212–216.

SHANKAR, S., RAMASWAMY, S., MARCHETTI, M. & BOWICK, M.J. 2018 Defect unbinding in active nematics. *Phys. Rev. Lett.* **121** (10), 108002.

SHENDRUK, T.N., DOOSTMOHAMMADI, A., THIJSSEN, K. & YEOMANS, J.M. 2017 Dancing disclinations in confined active nematics. *Soft Matter* **13** (21), 3853–3862.

SOKOLOV, A., ARANSON, I.S., KESSLER, J.O. & GOLDSTEIN, R.E. 2007 Concentration dependence of the collective dynamics of swimming bacteria. *Phys. Rev. Lett.* **98** (15), 158102.

TAN, A.J., ROBERTS, E., SMITH, S.A., OLVERA, U.A., ARTEAGA, J., FORTINI, S., MITCHELL, K.A. & HIRST, L.S. 2019 Topological chaos in active nematics. *Nat. Phys.* **15** (10), 1033–1039.

THAMPI, S.P., GOLESTANIAN, R. & YEOMANS, J.M. 2013 Velocity correlations in an active nematic. *Phys. Rev. Lett.* **111** (11), 118101.

THIEN, N.P. & TANNER, R.I. 1977 A new constitutive equation derived from network theory. *J. Non-Newtonian Fluid Mech.* **2** (4), 353–365.

VARGHESE, M., BASKARAN, A., HAGAN, M.F. & BASKARAN, A. 2020 Confinement-induced self-pumping in 3D active fluids. *Phys. Rev. Lett.* **125** (26), 268003.

WIOLAND, H., LUSHI, E. & GOLDSTEIN, R.E. 2016 Directed collective motion of bacteria under channel confinement. *New J. Phys.* **18** (7), 075002.

WU, K.-T., HISHAMUNDA, J.B., CHEN, D.T., DECAMP, S.J., CHANG, Y.-W., FERNÁNDEZ-NIEVES, A., FRADEN, S. & DOGIC, Z. 2017 Transition from turbulent to coherent flows in confined three-dimensional active fluids. *Science* **355** (6331), eaal1979.

ZAREI, Z., BEREZNEY, J., HENSLEY, A., LEMMA, L., SENBIL, N., DOGIC, Z. & FRADEN, S. 2023 Light-activated microtubule-based two-dimensional active nematic. *Soft Matter* **19** (35), 6691–6699.

ZHANG, R., MOZAFFARI, A. & DE PABLO, J.J. 2021 Autonomous materials systems from active liquid crystals. *Nat. Rev. Mater.* **6** (5), 437–453.

ZHOU, S., SOKOLOV, A., LAVRENTOVICH, O. & IGOR, S. 2014 Living liquid crystals. *Proc. Natl. Acad. Sci. USA* **111** (4), 1265–1270.